Spatial structures in optical parametric amplification

A. Beržanskis,[1] W. Chinaglia,[2] L. A. Lugiato,[3] K.-H. Feller,[1] and P. Di Trapani[2]
[1]*Faculty of Physics and Medical Engineering, University of Applied Sciences, Tatzendpromenade 1b, D-07745 Jena, Germany*
[2]*INFM, Department of Chemical, Mathematical, and Physical Sciences, University of Insubria at Como, via Lucini 3, 22100 Como, Italy*
[3]*INFM, Dipartimento di Fisica, Via Celoria 16, 20133 Milano, Italy*
(Received 23 December 1998)

We analyze the spatial aspects of the down-converted field emitted by a cavityless optical parametric amplifier, both from theoretical/numerical and experimental viewpoints. Our model neglects pump depletion and includes a classical description of the noise which initiates the process. The ringshaped angular distribution in the far field is determined basically by the phase-matching conditions. In the near field, the configuration arises from the superposition of contributions from a broad frequency band; it is shown that the finite duration of the pump pulse introduces a correlation among neighboring frequencies that allows for the appearance of a spotlike spatial modulation. When the spatial configuration of the pump field is changed from a plane wave to a narrow Gaussian, the near-field pattern assumes the form of a roll structure. The experimental observations obtained with a lithium triborate crystal agree qualitatively well with the theoretical picture.
[S1050-2947(99)05608-5]

PACS number(s): 42.65.Sf, 42.65.Ky, 42.50.Ct

I. INTRODUCTION

The field of optical pattern formation has received great attention in the 1990s, both from the theoretical and the experimental viewpoint; some reviews can be found in [1–7]. Several kinds of configurations have been considered, e.g., unidirectional propagation, counterpropagating waves, systems with single feedback mirror, nonlinear media contained in optical cavities with planar or spherical mirrors, systems with field rotation in the feedback loop, and arrays of lasers.

In the case of unidirectional propagation, the analyses have focused on the case of cubic nonlinearities, using the nonlinear Schrödinger equation or generalizations thereof (see, e.g., [8–13]). On the other hand, there is a literature on quadratic media, but in the intracavity case, either for optical parametric oscillators [14–19] or second-harmonic generation [20].

In this paper we study pattern formation in a cavityless propagation in the quadratic media. A remark is now necessary on the fact that we use the name ''pattern'' to designate the spatial structures that arise in an optical parametric amplifier in the linear regime of negligible pump depletion. As a matter of fact, optical patterns arise spontaneously from homogeneous configurations as a consequence of the interplay between the nonlinearity of the dynamics and diffraction, and the nonlinearity plays a crucial role in selecting the pattern (e.g., stripes, hexagons, etc.) that arise beyond the threshold of the instability that activates the pattern formation [7]. However, the recent studies on quantum images [18,21] have pointed out that one can meet the formation of pattern even below instability threshold, in a regime that can be described by a linear or linearized equations. Such patterns work as a precursor of the structure that appears above threshold, and are entirely generated by quantum fluctuations, hence they are noisy and change from realization to realization [13,18,21]. The ''pattern'' we study in this paper belongs to this class.

Throughout the paper, we consider the simple configuration of a type I optical parametric amplifier (OPA) in which a pump field is down converted to a signal and an idler field. Even if we analyze only the simplest setting of an undepleted pump, so that the dynamical equations are linear, the problem is complex because starting from quantum noise the OPA emits a broadband spectrum of both temporal and spatial frequencies correlated by the phase-matching condition, which implies that each different frequency is emitted on a different cone centered around the axis of propagation. One may arise the question of whether this broadband character of the radiation allows for transverse pattern formation at all.

The linear parametric amplifier has been extensively analyzed in the literature (see, e.g., [21–24]); here we focus on the aspects of pattern formation. The selective amplification of the spatial frequencies leads to the appearance of noisy spatial patterns in the near field, and to the formation of the system of cones in the far field. We will analyze carefully the structure of this set of cones in order to describe the phenomenology of the system.

We study the problem both in the near and in the far field, both theoretically and experimentally, and compare the theoretical picture with the experimental findings. Especially, we analyze the variation of the spatial structures when the pump field is gradually changed from a quasi-plane-wave configuration to a narrow Gaussian beam. Because the process of pattern formation is initiated by quantum fluctuations, the research is intimately related to the field of quantum aspects of optical patterns, especially with the investigations on ''quantum images'' [18,21]. However, in this paper we will mainly focus on the classical aspects, and leave the analysis of the specific quantum features to future work.

In Secs. II and III we consider the case of the plane-wave pump and study in detail the angular dependence of the

emission as governed by the phase-matching conditions. We compare the results with the experimental data. Section IV is devoted to the analysis of the effects that arise when we gradually reduce the diameter of the Gaussian pump; theoretical and experimental transverse patterns are illustrated and compared.

II. UNDEPLETED MONOCHROMATIC PLANE-WAVE PUMP

The traveling-wave OPA pumped by an undepleted monochromatic plane wave is perhaps one of the most thoroughly investigated systems in nonlinear optics. This problem can be solved analytically, thus, both classical and quantum properties of the OPA radiation have been studied widely in literature [22,23]. Here we briefly review the main results, as they are necessary for our study.

The classical equations for a traveling-wave parametric amplifier in the Fourier transform space have the following form [25]:

$$\frac{dS(\omega_1,k_{1,x},k_{1,y},z)}{dz}=\sigma_1 A_p S^*(\omega_2,k_{2,x},k_{2,y},z)e^{i\Delta kz}, \tag{1}$$

$$\frac{dS(\omega_2,k_{2,x},k_{2,y},z)}{dz}=\sigma_2 A_p S^*(\omega_1,k_{1,x},k_{1,y},z)e^{i\Delta kz}. \tag{2}$$

S is the spatiotemporal Fourier transform of the electromagnetic field generated by the parametric down-conversion process,

$$S(\omega,k_x,k_y,z)=\frac{1}{(2\pi)^3}\int A(t,x,y,z)e^{i(\omega t-k_x x-k_y y)}dtdxdy, \tag{3}$$

where $A(t,x,y,z)$ is the complex field envelope, t is the time, and x, y are the transverse coordinates, z is direction of propagation, A_p is the pump (frequency ω_p), and σ_1, σ_2 are the coupling coefficients. We assume A_p real in what follows. Frequencies ω_1, ω_2 and wave vectors $\mathbf{k}_1$, $\mathbf{k}_2$ of the modes must obey the requirements

$$\omega_1+\omega_2=\omega_p, k_{1,x}=-k_{2,x}, k_{1,y}=-k_{2,y}, \tag{4}$$

where the subscripts denote the projections of the wave vectors to the appropriate coordinate axis. Usually the wave with higher (lower) frequency is referred to as the signal (idler) wave. The phase-mismatch parameter is denoted in Eqs. (1) and (2) by $\Delta k=k_p-k_{1,z}-k_{2,z}$ and is dependent on the frequencies and wave vectors of the modes (e.g., $k_{1,z}=[k^2(\omega_1)-k_{1,x}^2-k_{1,y}^2]^{1/2}$); k_p is the wave vector of the pump, which is a plane wave propagating in the direction z. By making the phase-mismatch frequency and wave vector dependent we take into account dispersion and diffraction effects.

The solution of Eqs. (1) and (2) for $z=L$, where L is the length of the crystal, is [22]

$$\begin{aligned}S(\omega_1,k_{1,x},k_{1,y},L)&=e^{\frac{i\Delta kL}{2}}\left\{\left(\cosh(\Gamma L)-\frac{i\Delta k}{2\Gamma}\sinh(\Gamma L)\right)S(\omega_1,k_{1,x},k_{1,x},0)\right.\\&\left.+\sqrt{\frac{\omega_1}{\omega_2}}\frac{\Gamma_m}{\Gamma}\sinh(\Gamma L)S^*(\omega_2,k_{2,x},k_{2,x},0)\right\},\end{aligned} \tag{5}$$

where

$$\Gamma=\sqrt{\Gamma_m^2-\Delta k^2/4},\quad \Gamma_m=\sqrt{\sigma_1\sigma_2}A_p. \tag{6}$$

In this way, the output field of the OPA $A(t,x,y,L)$ can be found by inverting Eq. (3).

In this paper we do not deal with quantum aspects and therefore we will treat $S(\omega,k_x,k_y,0)$ as a classical c-number δ-correlated noise. Precisely, we assume that $A(t,x,y,0)$ corresponds to a Gaussian δ-correlated noise in time and space such that $\langle A(t,x,y,0)\rangle=0$ and

$$\langle A(t,x,y,0)A(t',x',y',0)\rangle=0, \tag{7}$$

$$\langle A^*(t,x,y,0)A(t',x',y',0)\rangle=\eta\delta(t-t')\delta(x-x')\delta(y-y'),$$

where the parameter η scales the noise level. Hence from Eq. (3) we have that $\langle S(\omega,k_x,k_y,0)\rangle=0$ and

$$\langle S(\omega,k_x,k_y,0)S(\omega',k_x',k_y',0)\rangle=0, \tag{8}$$

$$\langle S^*(\omega,k_x,k_y,0)S(\omega',k_x',k_y',0)\rangle=\eta\delta(\omega-\omega')\delta(k_x-k_x')\delta(k_y-k_y').$$

With the help of Eqs. (5) and (8) we obtain

$$\begin{aligned}\langle S^*(\omega,k_x,k_y,L)S(\omega',k_x',k_y',L)\rangle&=\eta\delta(\omega-\omega')\delta(k_x-k_x')\delta(k_y-k_y')\\&\times\left\{\frac{\omega_p}{\omega_p-\omega}\frac{\Gamma_m^2}{\Gamma^2}\sinh^2(\Gamma L)+1\right\}.\end{aligned} \tag{9}$$

The complex gain parameter Γ determines the character of the mode growth. Modes for which Γ is real exhibit exponential growth, while the others for which the parameter is imaginary will evolve in oscillatory fashion. It follows from expression (6) of Γ that the spatiotemporal structure of the field is determined by the phase mismatch, i.e., only the modes for which $|\Delta k|<2\Gamma_m$ will be amplified exponentially. Figure 1 illustrates this situation. For a fixed temporal frequency ω the gain experienced by a certain transverse mode depends sharply on the angle α between the wave vectors of the mode and of the pump. This gain peaks around a certain angle $\alpha(\omega)$ which is determined by the condition of the perfect phase matching $\Delta k=0$. In that way, emission for such a frequency at the output of the OPA is concentrated in a narrow spatial band and is maximal on the cone identified by the

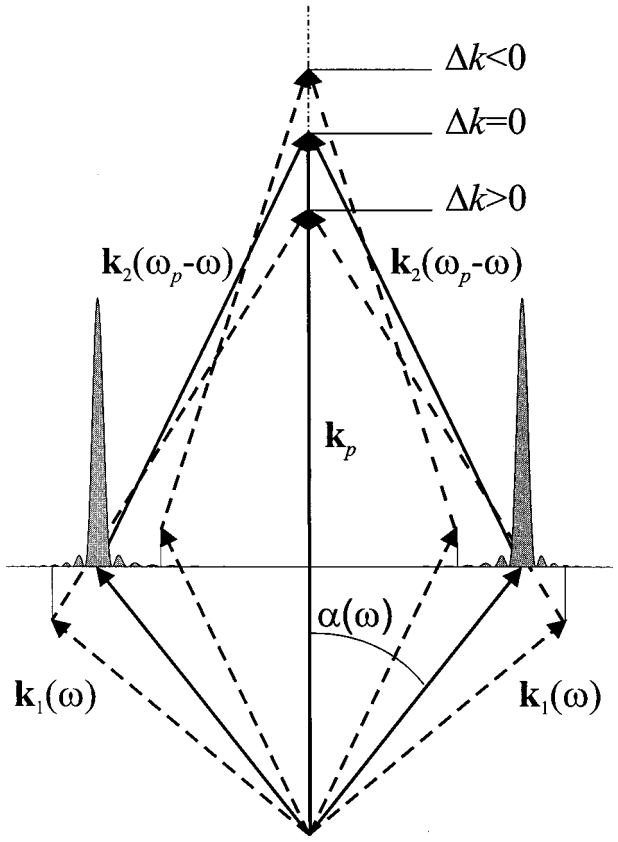

FIG. 1. Sketch of geometrical configuration of the wave vectors $\mathbf{k}_1$, $\mathbf{k}_2$, $\mathbf{k}_p$. For the given fixed temporal frequency ω the modes which propagate in angle $\alpha(\omega)$ with respect to the pump wave vector $\mathbf{k}_p$ exhibit a maximal exponential amplification. The angle is determined by the requirement of perfect phase-matching $\Delta k=0$.

condition $\Delta k=0$ (actually, there are two cones associated with each other, one for frequency ω and the other for frequency $\omega_p-\omega$) [22]. The perfectly phase-matched modes ($\Delta k=0$) experience the maximal gain Γ_m which is frequency dependent as the coupling coefficients σ_1, σ_2 depend on the temporal frequencies of the modes ω_1, ω_2 [Eqs. (1), (2)]. It can be approximately described as [25]

$$\Gamma_m=\sqrt{\frac{\omega_1\omega_2}{\omega_p^2}}\sigma A_p, \tag{10}$$

where the coefficient σ is independent of the frequency.

For a biaxial crystal, as we have in our experiment, the situation is more complex because the modulus of the wave vectors $\mathbf{k}_1$, $\mathbf{k}_2$ depends on their orientation. In this case, the set of wave vectors $\mathbf{k}_1$ which fulfills the perfect phase-matching condition $\Delta k=0$ is a cone with a section, in a plane orthogonal to the axis of propagation, which does not correspond to a circle but to an ellipse. Hence, if we denote by ϕ the angle identified by the transverse part of the wave vector in the orthogonal plane, we have that the angle of the perfect phase matching depends not only on ω but also on ϕ, i.e., $\alpha=\alpha(\omega,\phi)$.

III. ANGULAR SPECTRUM (FAR FIELD) OF THE BROADBAND OPA RADIATION

A. General considerations

The angular spectrum of an OPA pumped by a plane monochromatic wave has a cone structure for a fixed frequency. In a concrete situation the OPA operates over a broad band of temporal frequencies, i.e., each of these frequencies contributes to the emission. The intensity distribution of the broadband field, as we show here, is not uniform and may consist of one or a few sharp intense rings (or ellipses, for a biaxial crystal).

We consider a detector which measures the emission over a square of side $2l$ in the transverse plane $z=L$, and the time interval $-T<t<T$, so that the measured quantity is given by

$$M=\int_{-l}^{l}dx\int_{-l}^{l}dy\int_{-T}^{T}dt|A(t,x,y,L)|^2. \tag{11}$$

By using the inverse of Eq. (3) we obtain at once

$$\begin{aligned}M=&\int d\omega\int d\omega'\int dk_x\int dk_x'\int dk_y\\&\times\int dk_y'S^*(\omega,k_x,k_y,L)S(\omega',k_x',k_y',L)\times 2l\\&\times\operatorname{sinc}[(k_x-k_x')l]2l\operatorname{sinc}[(k_y-k_y')l]2T\\&\times\operatorname{sinc}[(\omega-\omega')T],\end{aligned} \tag{12}$$

where $\operatorname{sinc}(x)=\sin(x)/x$. With the help of Eq. (9) we can conclude that the average value $\langle M\rangle$ is given by

$$\begin{aligned}\langle M\rangle=&\int d\omega\int dk_x\int dk_y 8l^2T\eta\\&\times\left\{\frac{\omega_p}{\omega_p-\omega}\frac{\Gamma_m^2}{\Gamma^2(\omega,k_x,k_y)}\sinh[\Gamma(\omega,k_x,k_y)L]+1\right\}.\end{aligned} \tag{13}$$

Hence we can interpret that the intensity distribution in the variables ω, k_x, k_y is proportional to

$$I_s(\omega,k_x,k_y)=\frac{\omega_p}{\omega_p-\omega}\frac{\Gamma_m^2}{\Gamma^2(\omega,k_x,k_y)}\sinh[\Gamma(\omega,k_x,k_y)L]+1. \tag{14}$$

Because k_x and k_y are the Fourier components in transverse plane, the function

$$\overline{I_S}(k_x,k_y)=\int I_S(\omega,k_x,k_y)d\omega \tag{15}$$

corresponds to the intensity distribution in the far field. Since $k_x=|\mathbf{k}(\omega,\alpha,\phi)|\sin(\alpha)\cos(\phi)$, $k_y=|\mathbf{k}(\omega,\alpha,\phi)|\sin(\alpha)\sin(\phi)$, we can consider instead of $\overline{I_S}(k_x,k_y)$ the quantity

$$\overline{I_S}(\alpha,\phi)=\int I_S(\omega,k_x(\omega,\alpha,\phi),k_y(\omega,\alpha,\phi))d\omega, \quad (16)$$

which corresponds to the angular intensity distribution in the far field.

In order to get a feeling about the features of the angular spectrum $\overline{I_S}(\alpha,\phi)$ we take into account that for a certain frequency ω and angle ϕ the quantity $I_S(\omega,\alpha,\phi)$ is sharply peaked around the value $\alpha(\omega,\phi)$ for which there is perfect phase matching, so that we can approximate

$$I_S(\omega,k_x,k_y)=I_S(\omega,\alpha,\phi)\sim I_S(\omega,\alpha(\omega,\phi),\phi) \times\delta(\alpha-\alpha(\omega,\phi)). \quad (17)$$

For the sake of simplicity, let us neglect the dependence on ϕ. In our case, the ellipticity is quite negligible (about 5%) for the values of the angle α we are dealing with, so that we can reasonably approximate by assuming a cylindrical symmetry around the pump wave vector axis. Hence, we obtain from Eqs. (16), (17)

$$I_S(\alpha)=\sum_i I_S(\omega_i(\alpha),\alpha)\left|\frac{d\omega_i}{d\alpha}\right|, \quad (18)$$

where $\omega(\alpha)$ is the inverse of the function $\alpha(\omega)$ and the sum takes into account the fact that the function $\omega(\alpha)$ is multivalued in general, i.e., modes of different temporal frequencies are propagating at the same angle, thus, we have to sum up these temporal frequencies.

Equation (18) shows that the overall intensity of the far field is formed by each of the temporal frequencies independently while the broadband character of the radiation is accounted for by the factor $|d\omega(\alpha)/d\alpha|$ (density of the modes per angle α). In order to study the properties of this factor we must come back to the phase-matching conditions.

B. Phase-matching features, lithium triborate crystal

To find out the angular spectrum of the broadband OPA radiation we analyze in more detail the dependence of the phase-mismatch term Δk on the mode wave length (the dependence on the wave vector orientation was studied in Sec. II).

We indicated by x, y, z a Cartesian set of coordinates, with z being the direction of propagation of the pump. We now introduce another set of coordinates X, Y, Z which corresponds to the axes of the crystal, such that the main refractive indices obey the inequality $n_X<n_Y<n_Z$ (Fig. 2). We indicate by Θ and Φ the polar angles with respect to this coordinate system. In our experiments we use a lithium triborate (LBO) crystal, cut for type I phase matching at $\Theta=90°$, $\Phi=11.6°$, hence we will use the dispersion parameters of LBO further in our theoretical study (for the details, see the Appendix, in which Θ and Φ denote the polar angles for a generic wave vector $\mathbf{k}$). The wavelength of the pump is $\lambda_p=0.5275\ \mu$m. In the following, we indicate by Θ_p, Φ_p the polar angles for the pump wave vector $\mathbf{k}_p$, and we will always take $\Theta_p=90°$.

To demonstrate that noncollinear generation is possible in the crystal we show the phase mismatch $\Delta k_{||}$ for the collinear configuration of the wave vectors $\mathbf{k}_1$, $\mathbf{k}_2$, $\mathbf{k}_p$ for different orientations, Φ_p, of the crystal in Fig. 3. The collinear generation takes place at the wavelength for which $\Delta k_{||}=0$. On the other hand, noncollinear generation is possible if $|\mathbf{k}_1|+|\mathbf{k}_2|>|\mathbf{k}_p|$ (see Fig. 1). This argument is clear if we neglect the angular dependence of $\mathbf{k}_1$ for fixed ω_1, but remains basically true in general. The latter requirement can be rewritten as

$$\Delta k_{||}<0. \quad (19)$$

Figure 3 shows that for a proper orientation of the crystal there exists an interval of wavelengths where the condition

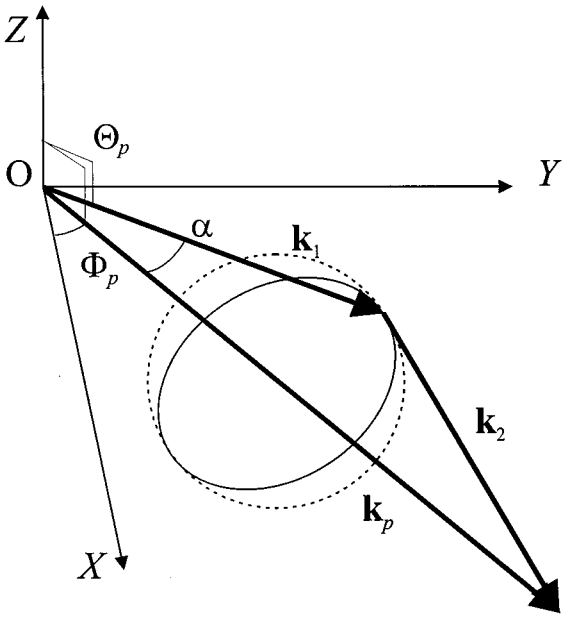

FIG. 2. Definition of the crystal orientation angles Θ_p and Φ_p; the axes of the crystal OX, OY, OZ are determined by requirement $n_X<n_Y<n_Z$ for the main refractive indices. The end of the wave vector $\mathbf{k}_1$ for the perfectly phase-matched modes draws a contour which is close to a circle. The angle α is defined to be in the plane $\Theta=90°$ in the text.

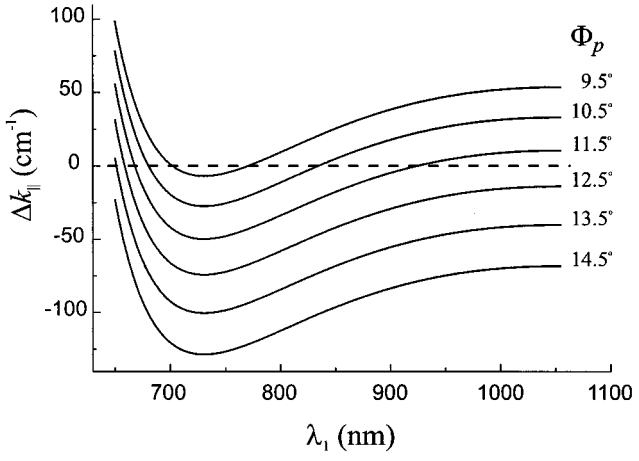

FIG. 3. Phase mismatch $\Delta k_{||}$ for the collinear orientation of the signal, idler, and pump wave vectors for different orientations of the crystal, Φ_p. Noncollinear generation is possible within the interval where $\Delta k_{||}<0$.

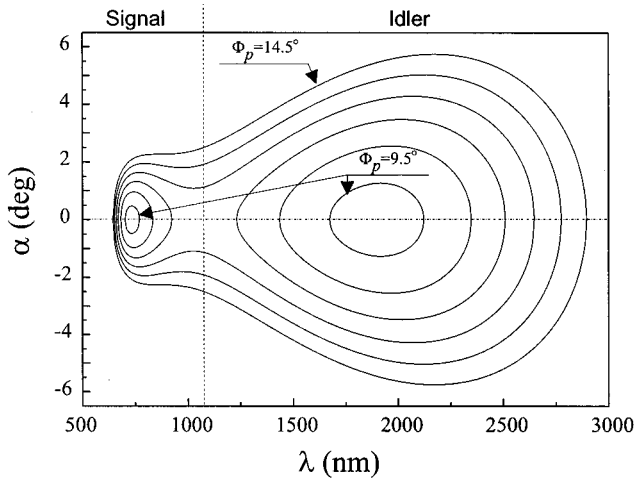

FIG. 4. Phase-matching curves for noncollinear generation in LBO crystal for different orientations of the crystal, Φ_p, $\Theta_p=90°$.

(19) is fulfilled, and noncollinear generation may be observed for the modes with the wavelengths within this interval.

For a given crystal orientation Φ_p with respect to the incident pump, parametric down conversion is generated at all angles and all wavelengths which fulfill the phase-matching requirements. The angle α versus the wavelength for the perfectly phase-matched modes is shown in Fig. 4 for the case described in the Appendix. Because in a biaxial crystal the angle $\alpha(\omega)$ also depends on the orientation of $\mathbf{k}_1$ as we said, in Fig. 4 we plot, for definiteness, the value of α when $\mathbf{k}_1$ lies in the plane XY. For the crystal orientations $\Phi_p=9.5°$, 10.5°, and 11.5° (Fig. 4) the angle α rapidly increases with the wavelength, it reaches a maximum value, and finally decreases slowly on approaching the edge of the tuning curve. Therefore, the density of temporal modes has a peak just at the limit angle where $\alpha(\lambda)$ has the maximum. Actually, the derivative $|d\omega(\alpha)/d\alpha|$ has a singularity of type $1/\sqrt{\alpha_{\max}-\alpha}$ at this point and so the density of the temporal

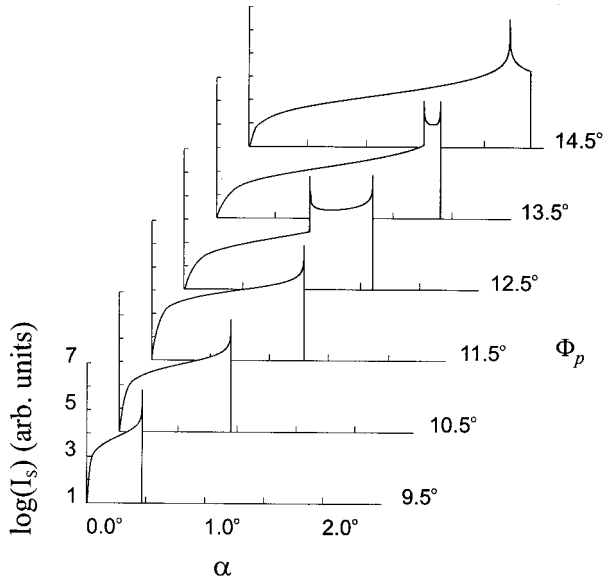

FIG. 5. Transverse angular spectrum. Pump wave intensity of 4 GW/cm^2 was taken.

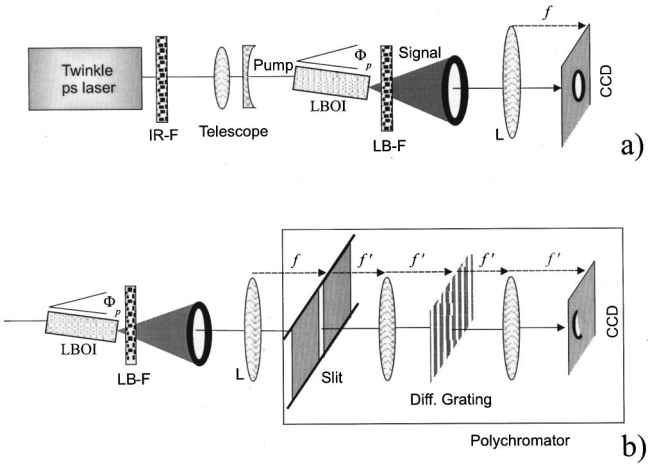

FIG. 6. Setup for the detection of (a) the energy angular distribution of the broadband signal-wave radiation; (b) the wavelength-on-angle dependence along the vertical diameter of the signal-radiation cone.

modes diverges [i.e., $d\alpha(\lambda)/d\lambda$ is zero], see Fig. 4. However, this singularity is integrable; it is in fact an artifact of our forcing an exact phase-matching condition [Eq. (17)]. Note that the wavelength $\lambda=1.055$ μm corresponds to degenerate emission. Hence the part of Fig. 4 on the left of the vertical line refers to the signal wave, the part on the right to the idler wave. For $\Phi_p=12.5°$, 13.5°, and 14.5° (Fig. 4) the two parts merge into single connected lines.

The intensity $\overline{I_S}(\alpha)$ is shown in Fig. 5. Equations (14), (16), (17) were used to get the results presented in the figure [we confined ourselves to modes of the signal wave ($\lambda<1.055$ μm) and neglected the contribution of the idler wave]. It is worth noting that for $\Phi_p=9.5°$, 10.5°, and 11.5° (Fig. 5) the angular distribution of the intensity has one peak, which corresponds to a ring of strong intensity. On the other hand, for the crystal orientations $\Phi_p=12.5°$ and 13.5° (Fig. 5) the angular distribution has two peaks. This is due to the peculiarities of the tuning curves for this orientation of the crystal, i.e., the angle α has a maximum in the interval of wavelengths $0.7<\lambda<0.8$ μm and a minimum in the interval $0.8<\lambda<1.055$ μm. The angular intensity peaks both in the vicinity of the maximum and of the minimum as the density of the temporal modes has a singularity in both of them, thus, the radiation angular spectrum has double ring structure with different ''colors'' of the two rings.

The angular distribution of the idler wave ($\lambda>1.055$ μm) demonstrates similar features (see Fig. 4). The angle α which corresponds to the outer ring is larger than that of the signal wave.

C. Experimental results

The first part of the experiment is aimed at the characterization of the angular and wavelength intensity distribution of the radiation generated by a LBO-based OPA, operated in the regime of linear amplification (undepleted-pump approximation) and with large pump-beam diameter (plane-wave pump approximation).

The layout of the experimental setup is drawn in Fig. 6.

The pump source is a frequency-doubled, feedback-controlled mode-locked, chirped-pulse amplified Nd:glass la-

ser (model TWINKLE, produced by Light Conversion, Vilnius), delivering $\simeq$ 1 ps single pulses at 527 nm, with transform-limited spectral bandwidth, energy up to 2.5 mJ, and repetition rate of 2.5 Hz.

The filter IR-F represents a set of infrared absorbing filters (total transmission at 1055 nm less than 10^{-12}), whose function is that of eliminating any residual radiation at the laser-fundamental wavelength, which could compete with the quantum noise in seeding the OPA. The *Telescope* collimates the laser beam down to 0.5 mm full width at half maximum (FWHM) diameter at the entrance of the OPA nonlinear crystal.

The nonlinear crystal is a 15 mm long lithium triborate sample, cut for type I phase matching at $\Theta=90°$, $\Phi=11.6°$ [this cut is suitable for room-temperature collinear second-harmonic generation from Nd:YAG (YAG denotes yttrium aluminum garnet) lasers]. The crystal, whose refractive indices are given in the Appendix, was oriented to have the pump polarization in the XY plane and the signal/idler polarization along the Z axis, and mounted on a rotation stage which allowed it to rotate along the Z axis (i.e., changing the Φ_p angle while keeping $\Theta_p=90°$). In this configuration, the signal and idler beams exhibit a lateral walkoff of about 1° with respect to the pump. Due to the large pump-beam diameter, this walkoff does not affect the angular gain profile. Since the pump-beam diffraction is also negligible, we can assume that our operating regime is well described in the plane-wave pump approximation.

The pump-pulse energy at the entrance of the nonlinear crystal was set to about 0.1 mJ. At the corresponding intensity of a few tens of GW/cm^2 the parametric quantum-noise amplification turned out to take place with total energy-conversion efficiency smaller than 1%, which makes the undepleted-pump approximation correct, in our case.

The energy angular distribution of the broadband signal-wave radiation was recorded by means of a silicon charge coupled device (CCD) camera, placed in the focal plane of a positive lens (L), behind the crystal. The pump-wave radiation was eliminated by a low-band-pass filter (LB-F), while the idler (at wavelengths larger than 1055 nm) was not detected due to the cutoff of the camera sensitivity in the IR.

The results are presented in the left column in Fig. 7, where the average over 40 shots is taken. The central column shows the same field received by eliminating the short-wavelength modes ($\lambda<0.8$ μm) by means of a suitable low-band-pass filter. This column is included to demonstrate the second inner ring which appears for some orientations of the crystal (see Fig. 5). This ring is built by modes whose wavelengths are in the region of low sensitivity of our CCD camera, thus, it cannot be seen without filtering. The results we obtained prove our expectation that the angular spectrum consists of one or two rings-outer and inner—due to the peculiarities of the phase-matching curves. We want to mention that even for very high intensities of the pump we observed a weak emission only in the inner part of the outer ring, but no signal was detected outside, in good agreement with our model.

In order to characterize the (temporal) spectrum of the signal wave and to monitor the wavelength-on-angle dependence along one diameter (the vertical) of the signal-radiation circle we placed a polychromator with the entrance slit in the focal plane of the lens L, and the CCD camera on the back focal plane of the polychromator. In this way the entrance slit selects the signal radiation in the vertical plane, while the diffraction grating placed inside the polychromator separates the different spectral components in the horizontal plane. Since the entrance slit is in the far field of the signal radiation, and the CCD is in the image plane of the slit, the vertical position on the camera gives the vertical angular coordinate, leading to two-dimensional snapshots of the wavelength-on-angle distribution.

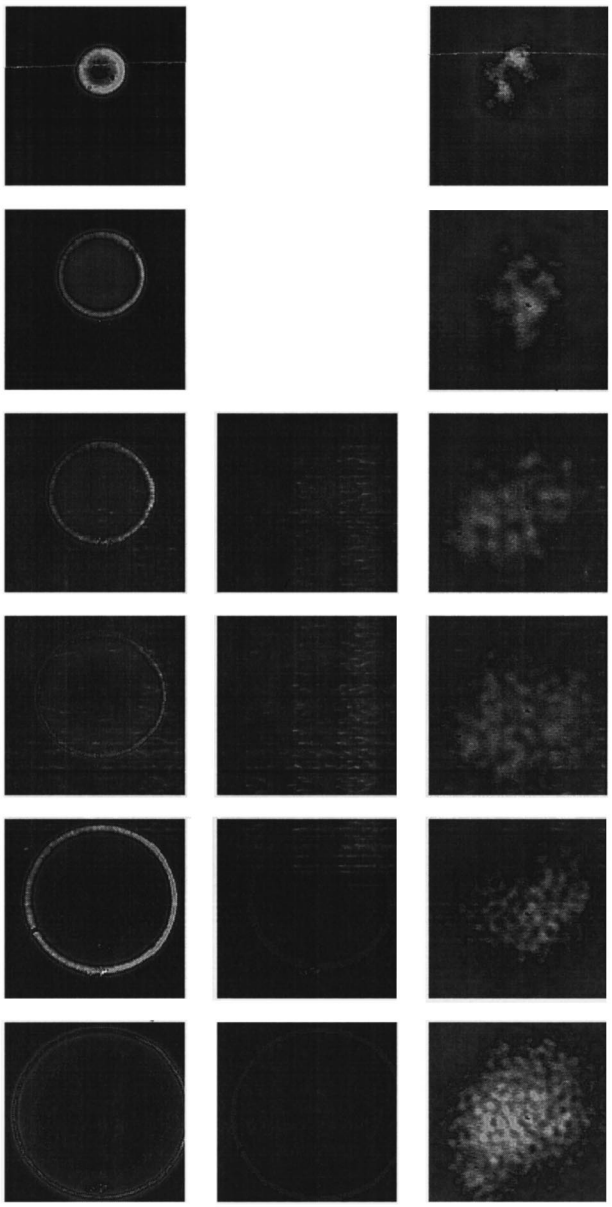

FIG. 7. Left column: Experimental far field of the OPA output; central column: the same after filtering the short-wavelength modes ($\lambda<0.8$ μm); right column: near field of the radiation. The values of angle Φ_p are (from top to bottom) $\Phi_p=9.5°$, $\Phi_p=10.5°$, $\Phi_p=11.5°$, $\Phi_p=12.5°$, $\Phi_p=13.5°$, $\Phi_p=14.5°$.

The resulting phase-matching curves, averaged over 40 shots, are shown in Fig. 8(a). The measured curves have finite ''thickness'' due to the influence of the nonperfectly phase-matched modes ($\Delta k\neq 0$) which are not taken into account in Fig. 4 [note that the gray scale in Fig. 8(a) is loga-

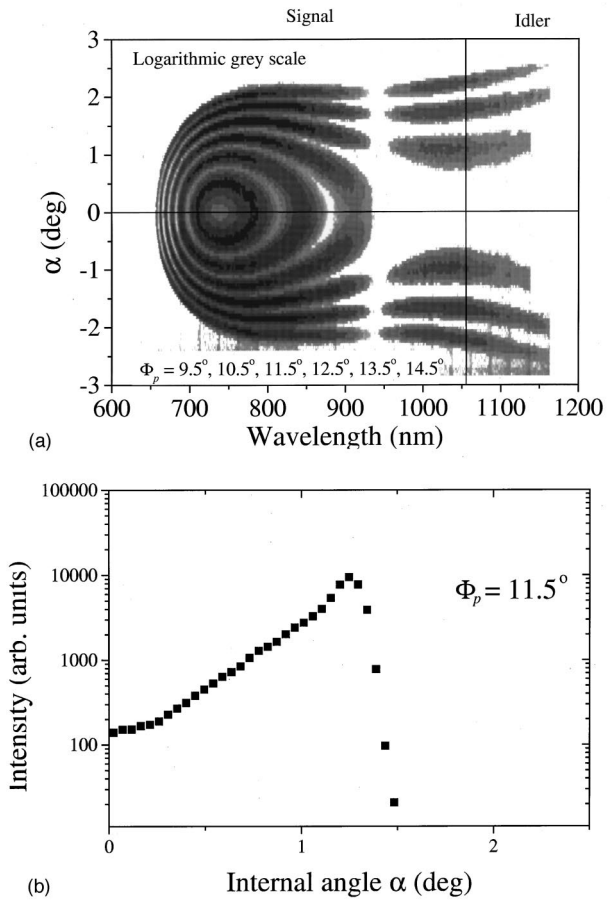

FIG. 8. (a) Experimentally measured phase-matching curves averaged over 40 shots (to be compared with the corresponding theoretical ones in Fig. 4). The thickness of the curves corresponds to the gain bandwidth (pump intensity 4 GW/cm^2). (b) Angular energy density at $\Phi_p = 11.5°$ obtained by integrating over wavelengths the corresponding data shown in (a).

rithmic]. As mentioned already, the sensitivity of our CCD camera enabled us to measure the region of the signal wave only. The intensity gap which is seen at the wavelengths 925–975 nm appeared because of the technical characteristics of our polychromator and is not really present in the radiation field. A good agreement is found between theoretically calculated curves and the experimental ones: the measured wavelengths for the maximal angle α coincide with the theoretical ones within the experimental error for all orientations Φ_p of the crystal. The radial energy distribution of the signal wave can be recovered by removing the polychromator, or equivalently by integrating the curves in Fig. 8(a) over the whole wavelength range. An example of such integration is shown in Fig. 8(b), for $\Phi_p = 11.5°$.

IV. NEAR FIELD. EFFECTS OF FINITE PUMP DURATION AND DIAMETER

A. Spatiotemporal correlation due to the finite pump duration and diameter

Here we turn our attention to the near field, which is the result of the interference of all the transverse modes, hence it is sensitive to the phase relations among the modes. The question of the correlation among the transverse modes becomes crucial when we discuss single-shot emission, both in the near and in the far field. In analyzing the angular intensity distribution in the preceding section we considered, instead, average quantities.

It is typical in the traveling-wave configuration that the detector integrates the intensity in time (especially if a pulsed pump is used). Thus, the detected transverse intensity distribution is a single shot in near field

$$I^T(x,y) = \int_{-T}^{T} dt |A(t,x,y,L)|^2, \tag{20}$$

where $2T$ is the detection time. If we take T on the order of the duration of the pump pulse, this is also a phenomenological way for introducing in our theory the pulsed nature of the pump. Our model, which assumes a stationary (monochromatic) pump, should be adequate to describe the results provided the pump pulse duration is much longer than the inverse of the bandwidth of the emission, as is the case in our experiment.

If we now introduce the Fourier transform in time,

$$\tilde{S}(\omega,x,y) = \frac{1}{2\pi}\int dt e^{i\omega t} A(t,x,y,L)$$
$$= \int dk_x dk_y e^{i(k_x x + k_y y)} S(\omega,k_x,k_y,L), \tag{21}$$

we obtain from Eq. (20)

$$I^T(x,y) = \int_{-\infty}^{\infty} d\omega \int_{-\infty}^{\infty} d\omega' \tilde{S}^*(\omega,x,y) S(\omega',x,y)$$
$$\times 2T \,\mathrm{sinc}[(\omega-\omega')T]. \tag{22}$$

Note that in the limit $T\to\infty$ we have $2T\mathrm{sinc}[(\omega-\omega')T] \to 2\pi\delta(\omega-\omega')$ so that

$$\lim_{T\to\infty} I^T(x,y) = 2\pi \int_{-\infty}^{\infty} d\omega |\tilde{S}(\omega,x,y)|^2 \tag{23}$$

is given by a superposition over all frequencies with the result of obtaining uniform intensity distribution in the near field, because the various waves have random phases, independent of one another. If we, instead, take T on the order of the pulse duration, the presence of the function $\mathrm{sinc}[(\omega-\omega')T]$ introduces a correlation among different frequencies, so that the frequency integration does not give a uniform intensity distribution and some modulation is seen in the near field.

In order to visualize the transverse intensity pattern in the near field we employ Eqs. (5), (21), (22) in our numerical simulations, assuming that the mode amplitudes $S(\omega,k_x,k_y,0)$ are Gaussian random quantities obeying Eq. (8).

On the other hand, the transverse intensity distribution in the far field can be obtained from the same stochastic realization by calculating the quantity

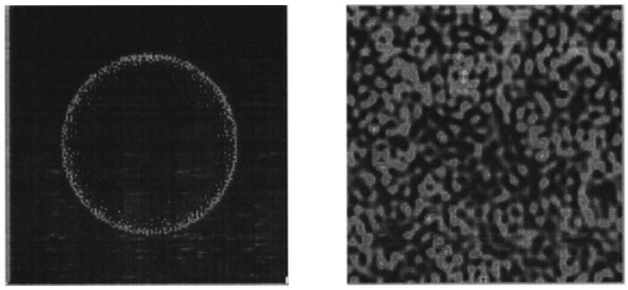

FIG. 9. Numerical simulation of the far- (left) and near- (right) field intensity distribution for a single shot, plane-wave pump. Pump intensity 4 GW/cm^2, $\Phi_p = 11.5°$. Pump pulse duration was taken to be 1 ps.

$$\int_{-\infty}^{\infty} d\omega \int_{-\infty}^{\infty} d\omega' S^*(\omega, k_x, k_y) S(\omega', k_x, k_y) \times 2T \mathrm{sinc}[(\omega - \omega')T]. \quad (24)$$

An example of the near-field and the far-field configuration, obtained in this way, is shown in Fig. 9.

Quite a regular structure is found in the near field of the radiation (Fig. 9). The pattern is seen over an intense uniform background which is caused by the averaging over the temporal frequencies. The contrast of the pattern (ratio of the intensity modulation amplitude with the background) is quite low (in the order of a few %). The transverse modes whose wavelengths are close to the one where the density of temporal modes peaks prevail in the pattern structure.

According to our model, the numeric simulation shows that increasing the correlation interval among the temporal modes (i.e., reducing T) increases the contrast of the pattern and vice versa. On the other hand, the contrast of the pattern can be increased sharply by filtering out some of the temporal frequencies. The same result can be achieved by seeding the OPA by a spatially noisy signal of a certain frequency. Figure 9 exhibits the numerically calculated single-shot far-field configuration, which is qualitatively similar to the experimental findings shown in Fig. 7 (left column).

We have shown before that the finite duration of the pump introduces a correlation among temporal frequencies. A similar effect arises in the spatial domain if we abandon the idealized assumption of the plane-wave pump. If we denote by $A_p(x,y)$ the spatial configuration of the pump, and introduce its Fourier transform

$$S_p(k_x, k_y) = \frac{1}{(2\pi)^2} \int dx dy e^{-i(k_x x + k_y y)} A_p(x,y), \quad (25)$$

in Eqs. (1), (2) one must introduce the following changes:

$$A_p S^*(\omega_2, k_{2,x}, k_{2,y}) \rightarrow \int dk_x' dk_y' S_p(k_x', k_y') \times S^*(\omega_2, k_x' - k_{2,x}, k_y' - k_{2,y}), \quad (26)$$

$$A_p S^*(\omega_1, k_{1,x}, k_{1,y}) \rightarrow \int dk_x' dk_y' S_p(k_x', k_y') \times S^*(\omega_1, k_x' - k_{1,x}, k_y' - k_{1,y}). \quad (27)$$

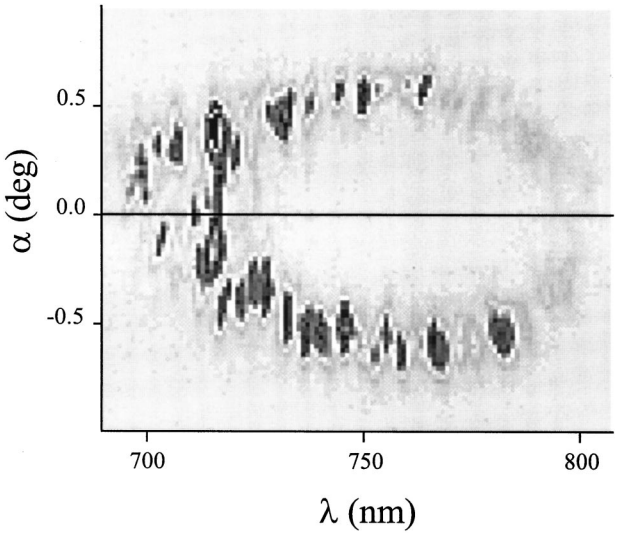

FIG. 10. Experimental single-shot angular-wavelength dependence, $\Phi_p = 9.5°$. One notes the spatiotemporal correlation introduced due to the finite pump pulse beam duration and diameter.

Hence the spatial dependence of the pump introduces a correlation among different spatial frequencies; the correlation is introduced by the convolution terms in Eqs. (26), (27).

B. Further experimental results

First, we present in Fig. 10 the intensity angular-wavelength distribution which was found under the same conditions as in Fig. 8(a) but for a single shot [Fig. 8(a) is obtained after averaging over 40 shots]. The picture shows the spatiotemporal correlation among the modes. One can see that the modes tend to group into spots of finite diameter and this is a trace of the spatiotemporal correlation among the modes. This behavior lets us expect to see a structure in the near field of the radiation.

The same experimental setup was used as described in Sec. III C. The near-field intensity distribution of the signal emission was obtained by imaging the exit face of the nonlinear crystal onto the CCD camera by means of suitable magnifying objective lenses.

The single-shot near-field intensity profile of the signal field is presented on the right-hand side of Fig. 11 (the corresponding angular spectrum is on the left-hand side). It is evident that the regular pattern structure (filamentation),

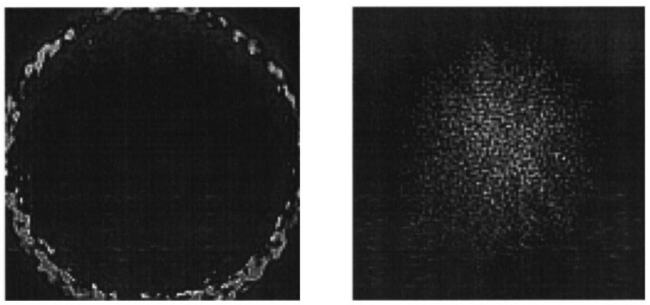

FIG. 11. Experimental far (left) and near field (starlike structure; right) of the OPA radiation for the pump-beam diameter 250 μm, $\Phi_p = 11.5°$ (pump intensity at the input 165 GW/cm^2, pulse duration 1.5 ps).

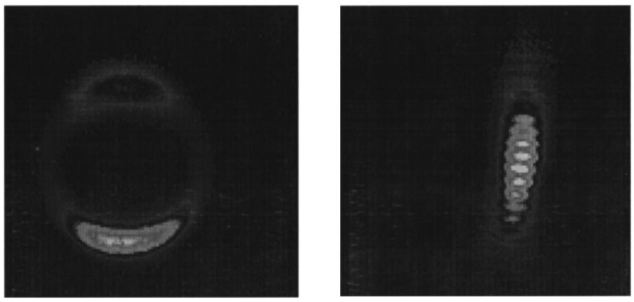

FIG. 12. Experimental far (left) and near field (right) of the OPA radiation for the pump-beam diameter 30 μm, $\Phi_p = 11.5°$ (pump intensity at the input 320 GW/cm^2, pulse duration 1.5 ps); roll-like structure.

whose details were changing from shot to shot (patterns are cancelled if averaged acquisition is taken) is present in the near field. Deeper analysis of the pictures shows that in the creation of the transverse modulation the spatial frequencies of the outer ring of the angular spectrum dominate, in agreement with our model. The characteristic spatial wavelength of the structure depends on the size of the ring (it decreases when the crystal is rotated in order to get larger rings in the angular spectrum).

We changed the pump-beam diameter by focusing the laser radiation in the crystal. Figure 11 presents the characteristic situation which appears when the pump-beam diameter is reduced. The angular spectrum ring becomes much broader and consists of a set of spots with quite noticeable radius. This is a consequence of the correlation introduced by the pump beam. In the near field we still find a pattern similar to the one we had in the plane-wave pump case. On the other hand, there are some differences. The pattern is limited in space by the pump beam and in the periphery the filaments tend to group on lines irradiating from the center of the pattern. In this way, the global view of the pattern resembles a star (Fig. 11).

The radius of the spots in the angular spectrum increases if the pump-beam diameter is reduced. In the absence of transverse walkoff, it would be possible to achieve the situation when the correlation radius is big enough to ''clean'' the angular spectrum completely, locking both the amplitudes and the phases of the modes on the whole ring. This would transform the starlike structure into a beam whose amplitude distribution is approximately described by a Bessel J_n function, as we have recently observed in the case of a type II LBO operated in noncritical phase matching [26]. With the present crystal, the walkoff plays a relevant role for pump-beam diameter smaller than a few hundred microns, selecting the angular components in the walkoff plane and leading to the far-field and near-field energy profiles shown in Fig. 12, whose stripe (roll) structure is similar to that predicted by models of optical parametric oscillators [14].

V. CONCLUSIONS

In the paper we made an overview of the spatial properties of the output radiation of the traveling-wave OPA. Because our analysis aimed at providing a qualitative picture rather than a quantitative comparison with experimental data, in our theoretical treatment for simplicity we used a classical description of the noise which initiates the emission, instead of a fully quantum picture.

We demonstrated that one or a few sharp rings appear in the far field of the broadband radiation of OPA. Such a structure of the angular spectrum is explained by the features of the phase-matching curves.

We showed that under appropriate conditions quite a regular spotlike transverse modulation can be seen in the near field of the output radiation. This modulation is preserved in spite of a very broad bandwidth of temporal frequencies which constitute the radiation though this broadband character results in quite a low contrast of the transverse modulation. The contrast depends on the correlation among the temporal modes of the radiation. It can be increased by using shorter pulses, by filtering the temporal spectrum of the radiation, or by seeding the OPA with a spatially incoherent but monochromatic field.

Finite pump diameter leads to correlation of neighboring spatial modes. As a consequence the angular spectrum of the radiation is ''cleaned.'' This changes the spatial properties of the near-field energy distribution. For a very small pump diameter roll-like structures can be generated from the quantum noise. Increasing the pump-beam diameter destroys these structures and leads to a starlike pattern. Further increase of the diameter smoothly transforms the starlike structures to the ones which are detected in the case of the plane-wave pump. Our experimental results show that the starlike configuration is characteristic for the intermediate diameters of the pump beam.

Finally, we found a good qualitative agreement between theoretical results and the experimental data obtained using a LBO crystal.

ACKNOWLEDGMENTS

The authors acknowledge G. Valiulis for providing the TLPI6 software which enabled us to calculate all necessary parameters of the nonlinear crystal. The authors are also grateful to S. Minardi for his help. This work has been done with the support of the Vigoni program and the MURST Project ''Spatial Pattern Control in Nonlinear Optical Systems,'' and the TMR Network Quantum Structures (QSTRUCT) of the EU.

APPENDIX: CALCULATION OF WAVE-VECTOR MODULO IN LBO CRYSTAL

The modulus of the wave vector of a plane wave of the wavelength λ propagating in a biaxial crystal is given by

$$|\mathbf{k}| = \frac{2\pi}{\lambda}\sqrt{\frac{b \pm \sqrt{b^2 - 4ac}}{2a}}. \tag{A1}$$

Here the minus sign stands for the fast wave (in our case—pump wave) and the plus sign stands for the slow waves (signal, idler). Coefficients a, b, c are

$$a = n_X^2 \sin^2(\Theta)\cos^2(\Phi) + n_Y^2 \sin^2(\Theta)\sin^2(\Phi) + n_Z^2 \cos^2(\Theta),$$

$$b = n_X^2(n_Y^2+n_Z^2)\sin^2(\Theta)\cos^2(\Phi) + n_Y^2(n_X^2+n_Z^2)\sin^2(\Theta)\sin^2(\Phi) + n_Z^2(n_X^2+n_Y^2)\cos^2(\Theta),$$

$$c = n_X^2 n_Y^2 n_Z^2 .$$

The angles Θ, Φ determine the orientation of the wave vector in coordinate system X, Y, Z corresponding to the axes of the crystal.

The refractive indices n_X, n_Y, n_Z for the LBO crystal are expressed by the following Selmaier formulas [27]:

$$n_X^2 = 2.454\,14 + \frac{0.011\,249}{\lambda^2 - 0.011\,35} - 0.014\,591\lambda^2 - 6.6\times 10^{-5}\lambda^4,$$

$$n_Y^2 = 2.539\,07 + \frac{0.012\,711}{\lambda^2 - 0.012\,523} - 0.018\,54\lambda^2 - 2.0\times 10^{-4}\lambda^4,$$

$$n_Z^2 = 2.586\,179 + \frac{0.013\,099}{\lambda^2 - 0.011\,893} - 0.017\,968\lambda^2 - 2.2\times 10^{-4}\lambda^4.$$

[1] F. T. Arecchi, Physica D **51**, 450 (1991).
[2] L. A. Lugiato, Phys. Rep. **219**, 293 (1992).
[3] C. O. Weiss, Phys. Rep. **219**, 311 (1992).
[4] A. C. Newell and J. V. Moloney, *Nonlinear Optics* (Addison-Wesley, Redwood City, CA, 1992).
[5] L. A. Lugiato, Chaos Solitons Fractals **4**, 1251 (1992).
[6] W. J. Firth, in *Self Organization in Optical Application to Information Technology*, edited by M. A. Vorontsov and W. B. Miller (Springer-Verlag, Berlin, 1995).
[7] L. A. Lugiato, M. Brambilla, and A. Gatti, in *Optical Pattern Formation*, Advances in Atomic, Molecular and Optical Physics Vol. 40, edited by B. Bederson and H. Walther (Academic Press, New York, 1998), p. 229.
[8] M. Haelterman and A. Sheppard, Chaos Solitons Fractals **4**, 1731 (1994).
[9] Y. S. Kivshar and X. Yang, Chaos Solitons Fractals **4**, 174 (1994).
[10] C. T. Law and G. A. Swartzlander, Chaos Solitons Fractals **4**, 1759 (1994).
[11] N. Rosanov, Chaos Solitons Fractals **4**, 1759 (1994).
[12] R. Horak, J. Bajer, M. Bertolotti, and C. Sibilia, Phys. Rev. E **52**, 4421 (1995).
[13] E. M. Nagasako, R. W. Boyd, and G. S. Agarwal, Phys. Rev. A **55**, 1412 (1997).
[14] G. Oppo, M. Brambilla, and L. A. Lugiato, Phys. Rev. A **49**, 2028 (1994).
[15] S. Longhi, Phys. Rev. A **53**, 4488 (1996).
[16] S. Longhi, Phys. Rev. A **56**, 2397 (1997).
[17] G. Valcarcel, K. Staliūnas, E. Roldan, and V. Sanchez-Morcillo, Phys. Rev. A **54**, 1609 (1996).
[18] A. Gatti, H. Wiedemann, L. A. Lugiato, I. Marzoli, G.-L. Oppo, and S. M. Barnett, Phys. Rev. A **56**, 877 (1977).
[19] M. Le Berre, D. Leduc, S. Patrascu, E. Ressayre, and A. Tallet, Chaos, Solitons and Fractals **10**, 627 (1999).
[20] C. Etrich, U. Peschel, and F. Lederer, Phys. Rev. Lett. **79**, 2454 (1997).
[21] A. Gatti, L. A. Lugiato, G. L. Oppo, R. Martin, P. Di Trapani, and A. Beržanskis, Opt. Express **1**, 21 (1997).
[22] A. Sukhorukov and A. K. Shchednova, Zh. Éksp. Teor. Fiz. **60**, 1251 (1971) [Sov. Phys. JETP **33**, 677 (1971)].
[23] B. R. Mollow, Phys. Rev. A **8**, 2684 (1973).
[24] F. Devaeux and E. Lantz, J. Opt. Soc. Am. B **12**, 2245 (1995).
[25] Y. R. Shen, *The Principles of Nonlinear Optics* (Wiley, New York, 1984).
[26] P. Di Trapani, A. Beržanskis, S. Minardi, S. Sapone, and W. Chinaglia, Phys. Rev. Lett. **81**, 5133 (1998).
[27] V. G. Dmitriev, G. G. Gurzadyan, and D. N. Nikogosyan, *Handbook of Nonlinear Optical Crystals* (Springer-Verlag, Berlin, 1991).